Rapid and Facile Synthesis of Gold Trisoctahedrons for Surface-Enhanced Raman Spectroscopy and Refractive Index Sensing

Guili Zhao, Florian Lochon, Kassiogé Dembélé, Ileana Florea, Alexandre Baron, Razvigor Ossikovski, Aleix G Güell

ACS APPLIED NANO MATERIALS

www.acsanm.org
Article

Rapid and Facile Synthesis of Gold Trisoctahedrons for Surface-Enhanced Raman Spectroscopy and Refractive Index Sensing

Guili Zhao, Florian Lochon, Kassiogé Dembélé, Ileana Florea, Alexandre Baron, Razvigor Ossikovski, and Aleix G. Güell*

Cite This: ACS Appl. Nano Mater. 2024, 7, 5598−5609
Read Online

ABSTRACT: Au trisoctahedrons (TOHs) with sharp tips and high-index facets have exceptional properties for diverse applications, such as plasmon-enhanced spectroscopies, catalysis, sensing, and biomedicine. However, the synthesis of Au TOHs remains challenging, and most reported synthetic methods are time-consuming or involve complex steps, hindering the exploration of their potential applications. Herein, we present a facile and fast approach to prepare Au TOHs with high uniformity and good control over the final size and shape, all within less than 10 min of synthesis, for surface-enhanced Raman spectroscopy (SERS) and refractive index sensing. The size of the Au TOHs can be easily tailored over a wide range, from 39 to 268 nm, allowing a tuning of the plasmon resonance at wavelengths from visible to near-infrared regions. The exposed facets of the Au TOHs can also be varied by controlling the growth temperatures. The wide tunability of size and exposed facets of Au TOHs can greatly broaden the range of their applications. We have also encapsulated Au TOHs with zeolite imidazolate framework (ZIF-8), obtaining core−shell hybrid structures. With the ability to tune Au TOH size, we further assessed their SERS performances in function of their size by detecting 2-NaT in solution, exhibiting enhancement factors of the order of 10^5 with higher values when the LSPR is blue-shifted from the laser excitation wavelength. Au TOHs have been also compared for refractive index sensing applications against Au nanospheres, revealing Au TOHs as better candidates. Overall, this facile and fast method for synthesizing Au TOHs with tunable size and exposed facets simplifies the path toward the exploration of properties and applications of this highly symmetrical and high-index nanostructure.

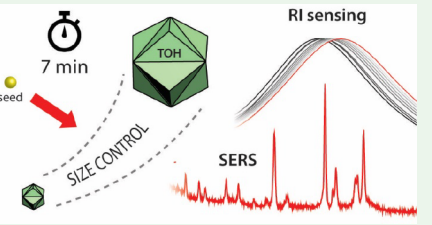

KEYWORDS: *Au trisoctahedrons, high-index facets, sharp tips, plasmonic nanoparticles, ZIF-8, SERS, refractive index sensing*

1. INTRODUCTION

In recent decades, significant attention and research efforts have been devoted to the preparation of Au nanostructures with controllable shapes, as there is a strong correlation between their morphologies and properties.[1−8] Nanostructures with high-index facets, possessing at least one of the three Miller indices larger than 1, are of particular interest due to their greater density of atomic kinks, steps, and edges, which often result in higher chemical-reaction activities compared to the low-index-faceted nanostructures.[9,10] Furthermore, high-index-faceted nanostructures exhibit a greater number of well-defined sharp tips and edges that present much stronger local electromagnetic fields, leading to more efficient surface-enhanced Raman scattering performances and higher sensitivities for sensing.[11,12] Despite their promising properties, synthesizing Au nanostructures with high-index facets remains a remarkable challenge because of their high surface energy, which causes fast atom deposition rates and makes these facets disappear during the growth process. As a result, nanoparticles tend to display low-index facets, such as {100}, {111}, and {110}, to minimize their surface energy.[13] Consequently, there is an extensive literature on various Au nanostructures with low-index facets, including nanocubes,[14] nanorods,[15,16] octahedrons,[17] and rhombic dodecahedrons.[18] In contrast, there are relatively few reports on Au nanostructures enclosed by high-index facets.[19,20]

The rapid advancements in the field of plasmonic nanostructures have enabled researchers to understand that the morphology of noble metal nanostructures is capable of being controlled through tuning the kinetic and thermodynamic growth conditions in wet-chemical methods.[21,22] This understanding has opened up possibilities for synthesizing nanostructures enclosed by high-index facets. Various morphologies have been successfully obtained, including tetrahexahedron with {hk0} facets, trapezohedron with {hkk} facets, trisoctahedron (TOH) with {hhl} facets, and hexoctahedron with {hkl} facets.[23] Among these, TOHs bounded by 24 triangular high-index facets possesses a high symmetry and exhibits only one dipolar plasmonic peak

Received: January 22, 2024
Revised: February 6, 2024
Accepted: February 7, 2024
Published: February 27, 2024

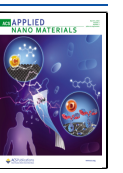

located between 500 and 800 nm, making them a suitable alternative in applications where Au nanospheres (NSs) are commonly used. For example, Xia's group demonstrated that Au TOH could provoke endocytic response with an efficacy comparable to that of Au NS.[20] Furthermore, the high-index facets of Au TOHs bestow to this nanostructure high catalytic performances, as reported in several works,[24,25] and its tipped surface makes it an excellent candidate for detection applications, such as surface-enhanced Raman spectroscopy (SERS).[26]

In 2008, Ma and coworkers first reported a wet-chemical method to synthesize Au TOHs enclosed by {221} facets,[9] highlighting the role of cetyltrimethylammonium chloride (CTAC) as the key surfactant. In spite of the fact that the method is simple, the limitations in tuning the size and the exposed facets called for the development of other synthetic approaches. In 2010, Yu et al. introduced seed-mediated methods on the synthesis of Au TOHs where the size can be tuned in a narrow range, providing the first control on the final nanoparticle size.[24] Other methods suitable for Au TOH synthesis have been followed with studies on shape evolution growth mechanisms,[26−30] but synthetic methods capable of controlling size in a wide range and exposed planes have yet to be developed. In 2015, Song et al. presented {331}-faceted TOHs with a remarkable range of sizes, from 60 to 255 nm, but through successive growths that might take more than a day to complete.[25] In 2018, Xia's group developed a new method with the ability to tune the dihedral angles by changing the reaction temperature;[20] however, the steps involved in this method are more complicated compared to other methods, and the tunable range of sizes is relatively narrow. We summarized the reported methods for preparing Au TOHs in Table S1.

Herein, we present a seed-mediated method to obtain Au TOHs that outperforms the procedures existing in the literature in three aspects. First, the synthesis process is simplified. This includes the preparation of seeds without a need for further treatment or aging time, as well as employing commonly used reagents and instrumentations. Second, we shortened the total reaction time to less than 10 min from start to end of the entire synthesis, including seed preparation. Third, the size of the resulting nanostructure can be controlled in a wide range from 39 to 268 nm by varying the volume of seed solution in the growth solution. Moreover, the Miller indices of facets for forming Au TOHs can also be tuned. Additionally, we demonstrated the synthesis of Au TOHs covered by zeolite imidazolate framework (ZIF-8), core−shell hybrid structures (Au TOH@ZIF-8) that pave the way to using this nanostructure in gas sensing[31,32] and catalysis applications. Finally, we demonstrated the applicability of Au TOHs for SERS and refractive index sensing. With this work, we ease the path of using high-index nanoparticles on a regular basis to explore their diverse applications, such as in photonics sensing, as herein demonstrated.

2. EXPERIMENTAL SECTION

2.1. Materials. Gold(III) chloride trihydrates ($HAuCl_4·3H_2O$, ≥ 99.9%), chloroplatinic acid hexahydrate ($H_2PtCl_6·6H_2O$, ≥ 99.9%), sodium borohydride ($NaBH_4$, ≥ 99.99%), L-ascorbic acid (AA, ≥ 99.5%), cetyltrimethylammonium bromide (CTAB, ≥ 99%), cetyltrimethylammonium chloride (CTAC, 25 wt % in water), 2-methylimidazole (2-MeIm, 99%), zinc nitrate hexahydrate ($Zn(NO_3)_2·6H_2O$, 99%), 2-naphthalenethiol (2-NaT, 99%), glycerol (≥99.5%), methanol (99.8%), and ethanol (99%) were purchased from Sigma-Aldrich. All the mentioned chemicals were used without further purification. Milli-Q water (resistivity 18.2 MΩ cm at 25 °C) was employed in all experiments.

2.2. Preparation of Au TOHs. Au TOHs were synthesized by a seed-mediated method. The first step was to prepare the seed solution by injecting freshly prepared ice-cold $NaBH_4$ solution (0.01 M, 900 μL) into a mixture of CTAB (0.1 M, 9.75 mL), $HAuCl_4$ (0.01 M, 150 μL) and H_2PtCl_6 solutions (0.01 M, 100 μL). A volume of 20 μL of the obtained seed solution was diluted into 10 mL of Milli-Q water. Depending on the final Au TOH size, a defined volume of the diluted seed solution was added to a mixed solution, which contains CTAC (25 mM, 10 mL), $HAuCl_4$ (0.01 M, 500 μL), H_2PtCl_6 (0.01 M, 5 μL), and AA solutions (0.1 M, 250 μL). The resulting mixture was kept undisturbed at 45 °C for 7 min, which was the time required for the reaction to complete.

2.3. Preparation of Au TOH@ZIF-8 Structures. The encapsulation of Au TOHs with ZIF-8 was carried out following a previously reported method[33] with minor modifications. Au TOHs were centrifuged twice (7000 rpm, 7 min) to remove CTAC and then redispersed in an aqueous solution of 1 mM CTAB. In 1 mL solution of 2-MeIm (1.32 M) at 35 °C with continuous stirring, 1 mL of an aqueous solution of $Zn(NO_3)_2·6H_2O$ (24 mM) was added, followed by the addition of 1 mL of washed TOH solution (in 1 mM CTAB) 1 min later. After 5 min of continuous stirring, the solution was left undisturbed until the collection of samples. The resulting Au TOH@ZIF-8 hybrids were centrifuged at 5000 rpm for 5 min and redispersed in methanol.

2.4. Characterization. The extinction spectra were collected on an Agilent Technologies Cary 60 UV−vis spectrophotometer. The scanning electron microscopy (SEM) images were obtained on a Hitachi S-4800 microscope. Transmission electron microscopy (TEM) imaging were performed on both JEOL 2010F microscope operating at 200 kV and FEI Titan Themis 300 G3 microscope operating at 300 kV. The selected area electron diffraction (SAED) patterns and high-resolution TEM (HRTEM) images were recorded on the FEI Titan Themis 300 G3. Scanning TEM (STEM) images were recorded using a high-angle annular dark-field (HAADF) and bright-field (BF) detectors; elemental mapping and energy-dispersive X-ray spectrometry (EDX) were acquired using a silicon drift detector from Oxford Instruments (X-Max 80T SDD). The 3-dimensional tomography data were acquired by using the serial EM acquisition software and a 4096 × 4096 pixels cooled CMOS Ceta camera. The tomography software allows for the automatic step-by-step variation of the tilt angle, the correction of the focus of the image, and the preservation of the object under study within the field of view. The tilt angle was varied in a range of −59° to +51°, and images were recorded every 2° giving a total of 56 images with a total acquisition time of about 10 min. The data treatment of the tilt series for preliminary image processing procedure was performed using the IMOD software. The volume reconstruction was obtained using 10 iterations of the algebraic reconstruction technique algorithm (ART)[34] implemented in the TOMOJ software.[35,36]

2.5. Finite-Element Method (FEM) Simulation. The simulated extinction spectra were computed using the finite-element-based commercial software COMSOL Multiphysics. A numerical model of the Au TOH was implemented by taking into account the experimental values of the geometry, including size and three projection angles α, β, and γ, obtained from the TEM images. The geometry of the TOH was smoothened on the edges and tips of the structure by resorting to cylinders and spheres. A smoothing of the tips with a spherical profile of radius r_s was set equal to the average size of the TOH divided by 40. The refractive index of Au was taken from Johnson and Christy's tables.[37] The host medium in which the particle is immersed is assumed to be water (with a nondissipative refractive index of 1.33). The simulated domain was defined as a sphere surrounded by perfectly matched layers to emulate an infinite medium. Maxwell's equations were solved in the scattered field formalism with the particle excited by an incident plane wave. The scattering cross section was computed by integrating the flux of the

https://doi.org/10.1021/acsanm.4c00455
ACS Appl. Nano Mater. 2024, 7, 5598−5609

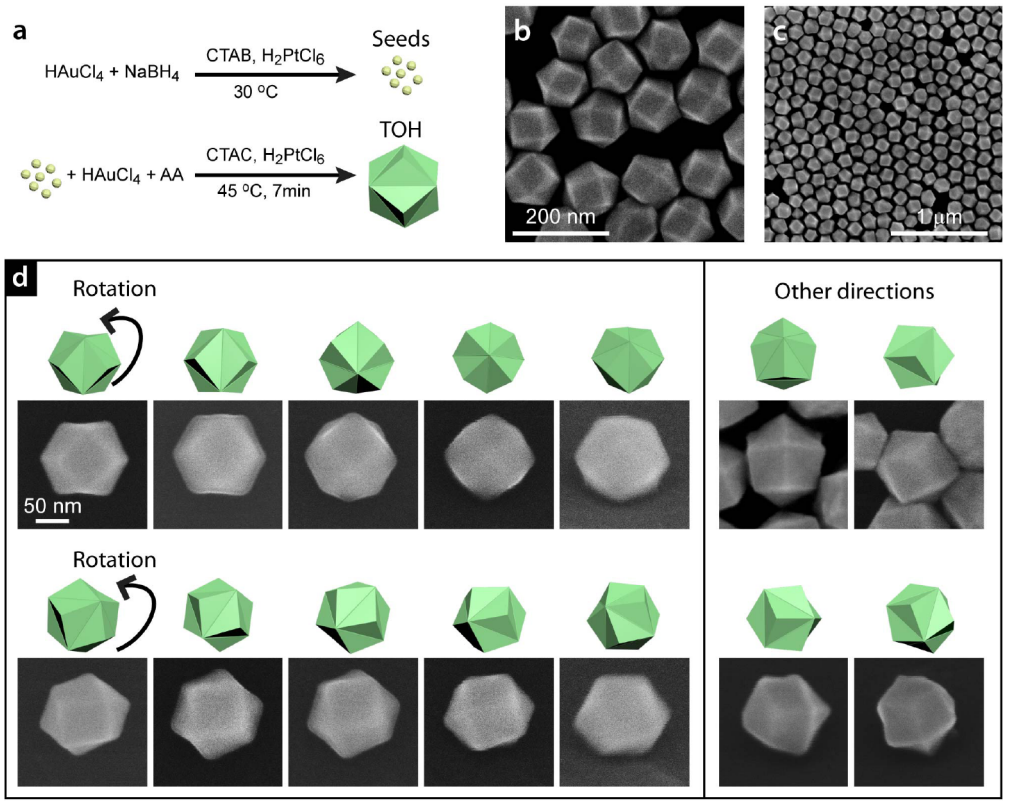

Figure 1. (a) Schematic of the procedure for the synthesis of Au TOHs: an initial step designed for the production of seed solution, followed by a seed-mediated growth step. (b, c) SEM images of the Au TOHs supported on a silicon substrate. The low-magnification image stresses on the monodispersity of the Au TOH size and shape. (d) Schematic models and SEM images of TOHs in different orientations. All the SEM images presented in (d) have the same scale bar.

Poynting vector of the scattered field across a closed sphere surrounding the particle and normalized to the input intensity. The absorption cross section was computed by integrating the ohmic losses over the entire particle volume and also normalized to the input intensity. The extinction cross section was taken as the sum of the scattering and absorption cross sections. It is worth noting that for every simulation, the extinction cross section was computed for three orthogonal directions of incidence of the impinging plane wave, obtaining negligible variations with orientation. However, the calculated electric field enhancements contour of a single particle was obtained by calculating a fixed orientation.

2.6. SERS Measurement. Three different Au TOH colloidal solutions were prepared with selected nanoparticle sizes, resulting in a localized surface plasmon resonance (LSPR) peak around the laser excitation wavelength while favoring the blue-shift zone, which is found to exhibit the highest Raman scattered signal.[26,38] The as-prepared Au TOHs (10 mL) were first washed twice with Milli-Q water to remove the surfactant as much as possible. Then the Au TOHs were redispersed into Milli-Q water (10 mL) and mixed with 2-NaT molecules dissolved into ethanol (20 μL, 0.01M), used as the Raman reporter. The resultant mixtures were left at room temperature for at least 2 h to ensure complete chemisorption. Subsequently, the mixtures were centrifuged to remove the unbounded molecules and redispersed into different volumes of Milli-Q water, thus obtaining a set of solutions with different Au TOH concentrations, ranging $\sim 10^7$ to $\sim 10^9$ NP mL^{-1} based on the measured extinction intensities and simulated cross sections. Raman spectra were collected with a confocal Raman microscope (LabRAM HR, HORIBA) equipped with a CCD camera (Synapse, HORIBA), a 633 nm HeNe laser, and a 600 grooves/mm diffraction grating. The spectra of colloidal solutions were collected employing a quartz cuvette with 1 cm optical length, a 3 mW laser power, a 10× objective lens (NA = 0.25), and an integration time of 20 s.

2.7. Refraction Index Measurements. The as-prepared Au nanoparticles were centrifuged and dispersed into Milli-Q water or the mixture of water and glycerol. The refractive indices of water and glycerol are 1.3334 and 1.4746, respectively. The volume percentage of glycerol in the water−glycerol mixtures was varied from 0% to 81% in steps of 9% to produce a gradual increase in the refractive index. The extinction spectra of these dispersion solutions of Au nanoparticles were recorded on the UV−vis spectrophotometer. Au NSs were synthesized following the seed-mediated method previously reported.[39]

3. RESULTS AND DISCUSSION

3.1. Synthesis and Characterization. As schematically shown in Figure 1a, Au TOHs were synthesized following a one-step seed-mediated method. The seed solution was obtained by mixing fresh ice-cold $NaBH_4$ solution with $HAuCl_4$, H_2PtCl_6, and CTAB solutions. The resulting solution was diluted into Milli-Q water and subsequently utilized as seeds for growing TOHs in the presence of CTAC, $HAuCl_4$, H_2PtCl_6, and AA as the surfactant, precursor, shape-directing agent, and reducing agent, respectively. The resulting products were first characterized by SEM imaging, to determine the morphology of the samples obtained. The TOH structure can be visualized as the resulting structure after 'pulling out' the centers of the eight triangular facets of an octahedron. Since three new faces are generated after 'pulling' one face, the TOH has a total of 24 faces. In Figure 1b,c representative SEM images of synthesized Au TOHs are shown, revealing the excellent match between the nanoparticle shape and the corresponding geometric model of TOH in Figure 1a. We noticed that the contours of some nanostructures are slightly

https://doi.org/10.1021/acsanm.4c00455
ACS Appl. Nano Mater. 2024, 7, 5598−5609

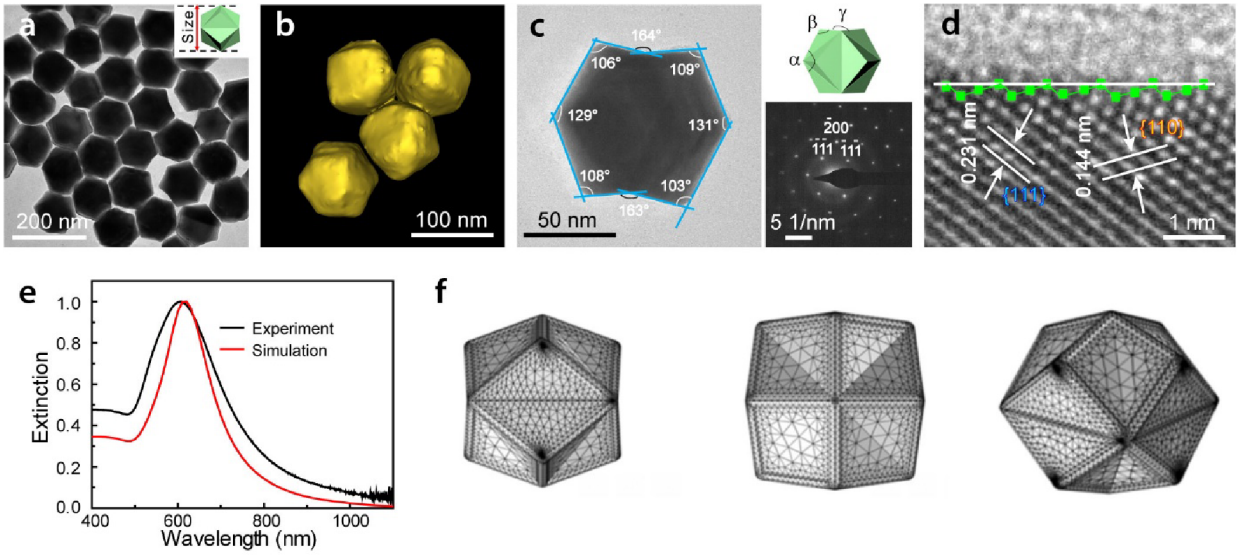

Figure 2. (a) TEM image of Au TOHs, emphasizing the sharp apexes of the structure. (b) Representative frame illustrating the 3-dimensional model of an ensemble of 4 Au TOHs obtained using the 3-dimensional Slicer software. (c) TEM image of a single Au TOH presenting a 94 nm size, recorded along the <110> direction. Inset in top-right is a schematic representation of an ideal TOH projected from the <110> direction. Inset in bottom-right is the corresponding SAED pattern. Measured projection angles between the various edges of the TOH are marked on the TEM image. (d) The corresponding HRTEM image of an edge-on facet allows the atomic steps on the surface to be identified. On the image, {111} steps and {110} terraces have been marked to highlight the {551} plane. (e) Normalized extinction spectra, experimentally obtained (black line) and simulated by FEM (red line), of Au TOHs with size of 123 ± 8 nm. (f) Typical meshing of the TOH structure used to compute the extinction cross section.

different at first glance. This difference is probably caused by their different projection orientations. This has been checked carefully rotating the sample during SEM observations. As shown in Figure 1d, a thorough comparison between high-magnification SEM images and the geometrical models confirms that most of the particles are indeed consistent with the TOH morphology but observed at different orientations. This visual effect has an inevitable impact on the measured size distribution (vide infra), yet the excellent size uniformity and high shape purity is appreciable in the SEM images.

In order to get more insights into the structural and morphological characteristics, TEM imaging was subsequently carried out. Figure 2a displays a representative low-magnification TEM image of the Au TOH obtained. The average size of the Au TOH along the longest axis (see the schematic inserted in Figure 2a for definition) measured from the TEM imaging was found to be 123 ± 8 nm. The wide size distribution was attributed to the deviation of the projection directions, for instance, the difference in the projection directions shown in the first two images in the top row of Figure 1d.

Furthermore, electron tomography studies were carried out on several nanoparticles, individual or assembled, in order to visualize their multifaceted 3-dimensional shape and tipped surfaces. The corresponding projection tilt series (Movie S1), as well as the reconstructed volume (see Movie S2) and how they were obtained are given in the Experimental Section. A representative frame of the tomography reconstruction model (see Movie S2) is shown in Figure 2b, presenting clearly the expected structural features of TOHs.

High-resolution TEM (HRTEM) was used to determine the Miller indices of the exposed facets in TOH structures. Since all the 24 facets belong to the crystal planes of the <110> zone axis family, the Miller indices are all {hhl}.[9] Two methods were considered. The first method involves measuring the projection angles when the TOH is viewed along the <110> direction, as described in Section 2 of the Supporting Information.[24,25] The angles are defined as α, β, and γ, respectively, as illustrated in the top right inset in Figure 2c. A typical TEM image of an individual TOH oriented along <110> axis is shown in Figure 2c, and the corresponding SAED pattern (bottom right inset) confirms the direction as well as the single-crystal nature of the particles. By comparing the measured projection angles with the calculated ones (Table S2), the Miller index of the facets enclosing the α angle is {331} and the ones enclosing the γ angle are close to {551} facets. The second method is by direct analysis of the arrangement of atoms on exposed facets from HRTEM images. Based on the step notion theory (Table S3), first reported by Van Hove and Somorjai,[40] the HRTEM image in Figure 2d illustrates that the Miller index of one edge-on facet is {551} since the facets are denoted by 3(110) × (111), matching well with the atomic model (Figure S1).

The optical properties of the synthesized Au TOHs were also examined. UV−vis spectrophotometry was carried out on the colloidal solutions to obtain the extinction spectra, as exemplified in Figure 2e. In this case, the extinction spectrum of Au TOHs with size of 123 ± 8 nm exhibits only one plasmonic peak, situated at 607 nm. We compared this experimental spectrum with a simulated one generated using the FEM modeling utilizing the morphologic parameters obtained from electron microscopy analyses. To ensure sufficient accuracy, the domain was meshed with elements that were small compared to the wavelength and the typical particle size (Figure 2f). A convergence study was conducted for each geometry, varying the number of meshed elements to ensure accuracy. This method has been used in the past to simulate the optical properties of various plasmonic nanostructures.[41,42] The simulation results, represented by the red

https://doi.org/10.1021/acsanm.4c00455
ACS Appl. Nano Mater. 2024, 7, 5598−5609

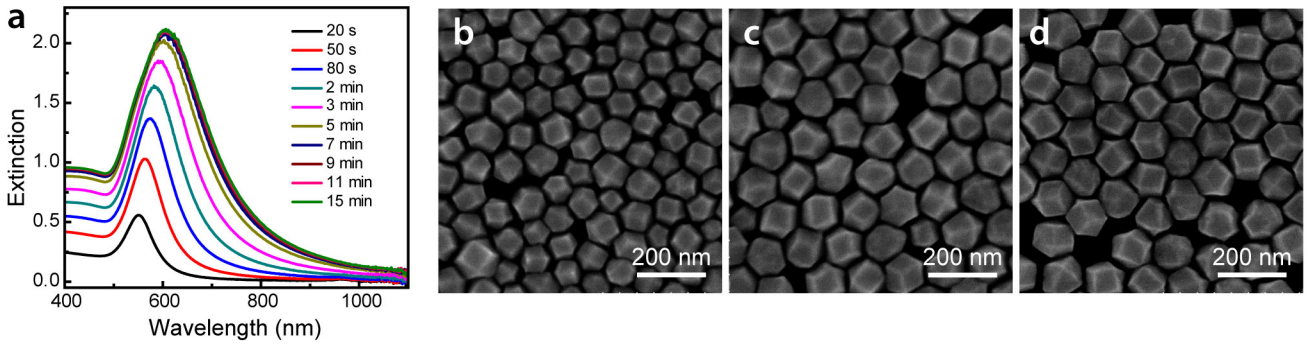

Figure 3. (a) Extinction spectra recorded at different growth times during the growth process of Au TOHs. (b–d) SEM images of the obtained products collected at 20 s, 3 min, and 7 min, respectively. It took 3 min to centrifuge each sample.

line in Figure 2e, also exhibit a single plasmonic peak at 620 nm, in agreement with the experimental results. The small deviation in the plasmonic wavelengths can be considered as a consequence of the slightly truncated tips in the as-prepared Au TOHs, which differs from the geometrical models used in the simulation. Additionally, we observed that the measured extinction band was broader than the simulated one. This difference is a result of the inhomogeneous Au TOHs, which possess a statistically size distribution around the mean value, but the size distribution is very narrow since the width is small.

To determine the total reaction time of our seed-mediated procedure, we considered the effect of prolonged reaction times in both the seed preparation and the growth step. Indeed, in seed-mediated growth methods, the formation of seeds can play a key role in determining the final morphology of the nanostructure, in some cases requiring also a post-treatment before being used in the growth step. This is exemplified in the synthesis of Au nanobipyramids where seeds need to be treated for 90 min at 80 °C.[43] Therefore, we first investigated how the final nanostructure changed as the time of seed formation was prolonged. The results, presented in Figure S2, showed that Au TOHs are obtained in high yield but differ in size. This size difference is associated with the decrease in the seed number in the seed solution by increasing the reaction time due to the Ostwald ripening effect.[44] Additionally, the excess of $NaBH_4$ in the seed solution has a negligible impact on the final shape since the original seed solution was diluted around 10^5 times. As a result, the seeds could be used immediately after the $NaBH_4$ was added, which largely shortened and simplified the entire synthetic procedure. We also monitored the morphology and size of the nanostructures at different growth times. The *in situ* extinction spectra recorded during growth, presented in Figure 3a, illustrate a unique plasmonic band with a continuous redshift over time as well as a gradual increase in peak intensity. After 7 min, the spectra at subsequent reaction times overlap, indicating that the growth process have finished. To determine if the nanoparticles evolve into different morphologies during growth,[28,29] samples were extracted at different growth times and immediately centrifuged to minimize any further growth outside the reactor. SEM images of the samples demonstrate that, even at the shortest reaction time of 20 s (and the 3 min of centrifugation), Au TOHs have already been formed. As the reaction time increased from 20 s to 7 min, only the size gradually increased while the morphology remained unchanged (Figure 3b–d). This combination of fast TOH formation and the immediate use of seed solution makes possible the complete synthesis of Au TOHs to be achieved in less than 10 min.

The formation of Au TOHs in high yield is strongly dependent on the composition of the solutions. We observed that adding H_2PtCl_6 in both the seed solution and the growth solution can greatly improve the quality of the Au TOHs. First, in the seed solution, the introduction of H_2PtCl_6 improved the monodispersity of the seeds, as we observed under TEM (Figure S3), and as was previously reported.[45] Seeds synthesized, diluted, and characterized with TEM under less than 20 min showed to be single crystals with dimensions ranging between 2 and 3 nm (Figure S3b). Additionally, seeds obtained using different ratios of $HAuCl_4$ and H_2PtCl_6 were employed for the synthesis of Au TOHs, confirming the role of H_2PtCl_6 in improving the monodispersity but with none or negligible effect on the morphology of the final Au nanostructures (Figure S4). For the growing stage, despite the small amount of H_2PtCl_6 added in the growth solution, a significant improvement in the shape purity of Au TOHs was noticeable (Figure S5). We assign this improvement to the fact that Pt atoms are preferentially deposited on the facets with high surface energy,[46] thereby blocking the growth of these facets and resulting in the formation of nanostructures with high-index facets rather than bipyramids with {11n} facets, which have low surface energy. The use of metal ions is a common practice to preferentially grow particular shapes and planes, although a clear mechanism is still part of an extended debate[47,48] due to the difficulty of distinguishing the individual role of metal ions in this preferential growth from other components present in the growth solution.[49,50] Importantly, elemental mapping and EDX carried out on the Au TOH obtained show that the TOH nanostructure is predominantly composed of Au element (Figures S6 and S7).

The type and concentration of surfactant also play a critical impact on the final nanostructure, as shown in previous studies.[9,25] The use of CTAC as the surfactant is beneficial for the formation of TOH in the absence of silver ions,[26,50] and therefore it was our first choice to use CTAC as the capping agent to prepare Au TOHs. We observed a significant influence of the CTAC concentrations on the final shape and size of the resulting nanoparticles, after carrying out a set of experiments with different concentrations of CTAC (Figure S8). The results indicate that high-purity TOHs can only be obtained when the concentration of CTAC is around 25 mM. We also confirmed that CTAB is not a suitable surfactant for the growth of Au TOHs under our experimental conditions (Figure S8h). The difference in products obtained by employing CTAC and CTAB as surfactants is caused by the

https://doi.org/10.1021/acsanm.4c00455
ACS Appl. Nano Mater. 2024, 7, 5598–5609

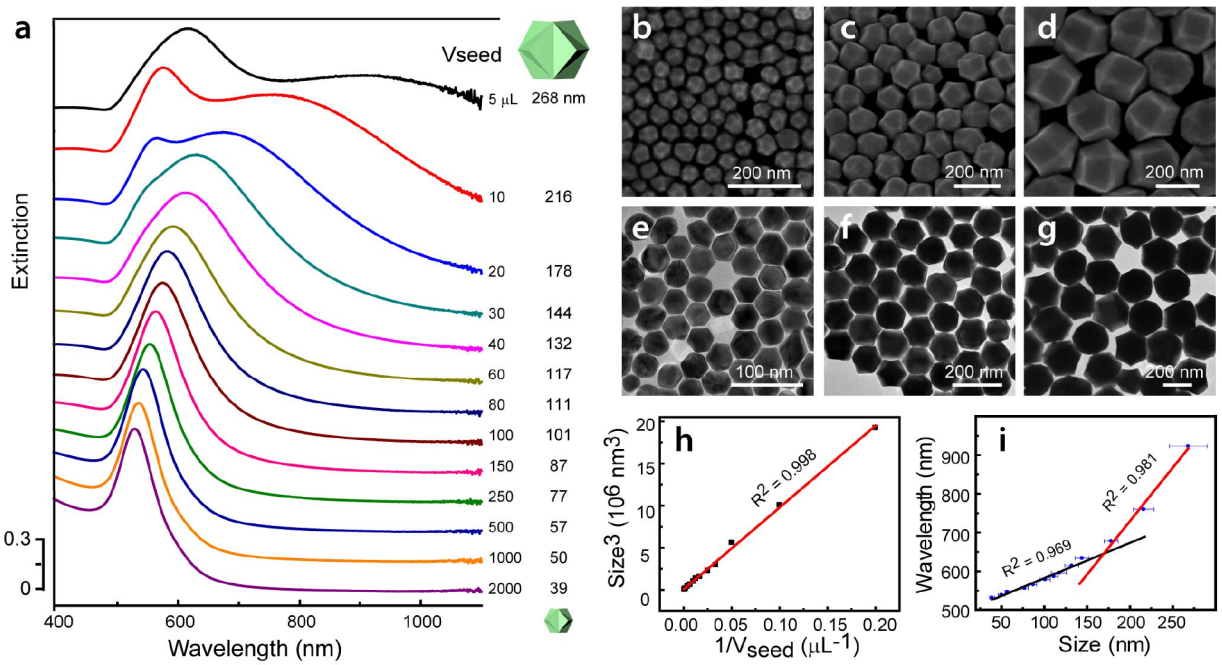

Figure 4. (a) Set of experimental extinction spectra of Au TOH colloidal solutions. The volume of seed solution used for each seed-mediated synthesis is indicated in the left column, together with the corresponding average size of the resulting TOH, right column. (b–d) SEM and (e–g) TEM images of representative samples. The images correspond to samples of 39 ± 3 nm, 132 ± 8 nm, and 268 ± 22 nm, respectively. (h) The linear relationship between the cubic power of the average size of TOHs and the reciprocal of the volume of the diluted seed solution in the growth solution. (i) The empirical double-linear relationship between LSPR dipolar peaks of Au TOHs and their sizes.

different affinities of these two surfactants. Generally, Br^- ions exhibit stronger binding to Au surfaces than Cl^- ions.[51]

High-index geometries as TOHs are obtained under kinetically controlled conditions, benefiting from a fast atom deposition rate in the synthesis and thus avoiding thermodynamically more stable planes with lower surface energy. Therefore, the amount of AA in the growth solution is an important factor for influencing the final nanostructures as the reducing rate of $HAuCl_4$ will increase when the amount of AA increases, resulting in a higher deposition rate of Au atoms. To understand how this affects the final nanoparticle shape and size, we conducted a series of experiments employing different amounts of AA in the growth solution while keeping other conditions constant. As shown in Figure S9, the formation of TOH shape requires a fast enough reduction rate to drive the growth not only on {110} facets but also on {111} and {100} facets, but at different growth rates. The optimal amount of AA (0.1 M) in our experiments is approximately 250 μL for 10 mL of growth solution.

3.2. Tuning TOH Size. The ability to synthetically tailor the LSPR properties through size control is one of the most outstanding features of Au nanostructures.[52,53] In seed-mediated growth methods, the final nanoparticle size can be easily fine-controlled by adjusting the amount of seed solution added into the growth solution while maintaining the other conditions constant.[43] We prepared 13 samples of Au TOHs by varying volumes of diluted seed solution, ranging from 2 mL to 5 μL. A digital photograph of these samples, shown in Figure S10, displays a variation of the colors of these 13 samples ranging from red to purple and finally brown as the amount of seed solution decreases. The extinction spectra of these 13 samples were acquired, presenting that the dipolar plasmon peak gradually red shifts from 532 to 923 nm (Figure 4a). The highly uniform shapes and sizes of these Au TOH samples were confirmed by SEM and TEM imaging, as shown in Figure 4b–g and Figures S11 and S12. The average size of Au TOHs measured from TEM images changes from 39 to 268 nm, with narrow size distributions that give standard deviations below 10% for any size of the range (Table S4). To the best of our knowledge, this is the broadest range of the Au TOH sizes synthesized in a one-step seed-mediated method. For larger Au TOHs, the extinction spectrum displays a broader dipole band as well as the appearance of the quadrupole mode band, as confirmed by FEM simulation (Figure S13), due to phase retardation effects.[39,54] A complete summary of the results is presented in Table S4, as well as the plots of the wavelength of dipolar plasmon peak and size versus the volume of the diluted seed solution (Figure S14). Interestingly, the third power of the TOH size is linearly related to the reciprocal of the volume of the diluted seed solution with a high fitting coefficient, as presented in Figure 4h. This observation is consistent with previous reports using seed-mediated methods,[39,55] demonstrating that Au atoms in the growth solution exclusively deposited onto the seeds without generating new nuclei, which is critical because the linearity would be disrupted if new nucleation occurred during synthesis. With the directly proportional relationship, it is very convenient to calculate the volumes of seed solution needed to synthesize Au TOHs with desired sizes. Previous works have reported the relationships between plasmonic peak and the size for Au NSs, Au nanorods, and Au nanobipyramids;[43,56] however, none has been established between dipolar plasmonic peak and size for Au TOHs. Herein, we plotted the dipolar plasmonic peak wavelength of Au TOHs as a function of their size (Figure 4i), drawing a double-linear behavior, trend that can be related to the variations in the volume of the nanostructures, as reported in previous works for other Au nanostructures.[43,57] This double-linear relationship is an

https://doi.org/10.1021/acsanm.4c00455
ACS Appl. Nano Mater. 2024, 7, 5598–5609

empirical observation that facilitates the selection of the experimental conditions for the synthesis of a Au TOH with a defined dipolar plasmonic band.

3.3. The Impact of Growth Temperature. In the process of the nanostructure growth, temperature can play a role in the rate of atom deposition[22] as well as in the atom mobility and rearrangement.[20] We evaluated the effect of different growth temperatures on the final nanostructures by carrying out a series of synthesis, from 25 to 95 °C. SEM and TEM imaging were performed to characterize the sizes and morphologies of the nanostructures obtained (Figure 5a–c, and Figures S15 and S16). The nanostructures formed at 25 and 45 °C are TOHs with an average size of 113 ± 6 and 114 ± 6 nm, respectively, but possess different average dihedral angles, 161 ± 3° and 163 ± 3°, respectively. This increase in dihedral angle indicates that the facet indices of nanostructures varied as the growth temperature increased, from around {441} for the synthesis at 25 °C to approximately {551} at 45 °C. As the growth temperature was further increased to 95 °C, atom mobility and rearrangement has a direct effect on the final nanoparticle morphology.[20] By carefully analyzing SEM and TEM images and comparing with schematic models, we confirmed that the morphology of the nanostructures obtained at 95 °C is mainly rhombic dodecahedron with {110} facets[48] instead of TOH, as shown in Figure 5c as well as Figures S15c,f and S16. This change in morphology also has an impact on the extinction spectra (Figure 5d), where a blue-shift in the LSPR peak is observed with an increase in the growth temperature. We ascribed the blue-shift in plasmonic peak to the variations in the Miller index, as the nanostructures became less sharp, which is in agreement with previous works.[11,58] To further confirm this, simulated extinction spectra of TOH enclosed by extreme planes {221} to {661} also exhibit a blue-shift as the Miller indices increase, shown in Figure 5e. The shift range in the simulation results is larger because the built TOH structure is sharper than the experimentally obtained TOH.

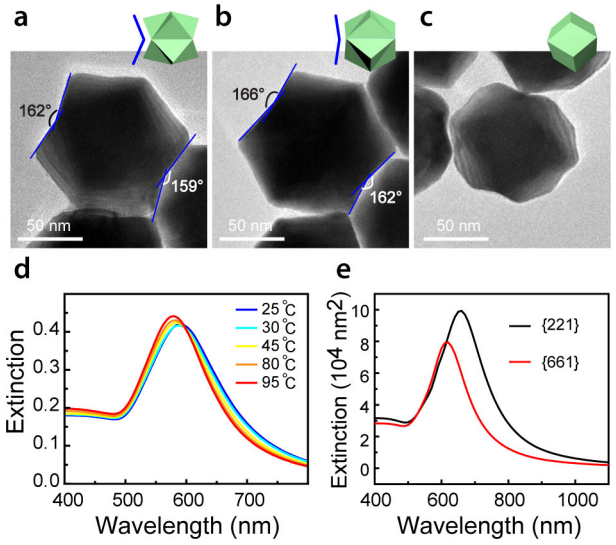

Figure 5. (a–c) TEM images of individual particles obtained at 25 °C, 45 °C, and 95 °C, respectively. The change in the dihedral angles measured proves a variation in the exposed high-index facets. An average data of 60 angles (30 particles) were measured for each sample on particles projected along the <110> direction. Insets of indicative geometric models are provided to illustrate the shape evolution for different temperatures, with the blue lines marking the change in dihedral angle. The TOH geometry is lost when the synthesis is carried out at high temperatures. (d) Extinction spectra of Au TOHs obtained at different growth temperatures. (e) Simulated extinction spectra for two extreme planes, {221} and {661} confirm the blue-shift observed in the experiment.

3.4. Encapsulation with Metal Organic Framework ZIF-8. Combining plasmonic nanoparticles with metal organic frameworks (MOFs) in a core–shell hybrid structure has been a recent approach to extend the applicability of SERS for the detection of gas.[31,32,59] For the encapsulation, CTAB has shown to play an important role as a bridge molecule to facilitate the attachment and posterior growth of ZIF-8 on the planes of the metal particle core.[33,60] To facilitate the interaction between Au TOHs capped with CTAC and ZIF-8, the as-prepared Au TOHs were washed twice in 1 mM CTAB before being encapsulated. This capping agent exchange led to an increase in the random attachment of formed ZIF-8 nucleus onto the surface of the Au TOH, as shown in Figures 6a and S17a). The subsequent growth of ZIF-8 was localized on the attached nucleus, leading to an asymmetrical structure (Figures 6b and S17b). The final core–shell Au TOH@ZIF-8 results in the expected cubic structure,[61] with a single metallic nucleus slightly off-centered (Figures 6c and S17c). The vast majority of the Au TOHs were encapsulated; however, the homogeneous nucleation of ZIF-8 taking place simultaneously generates a side population of cubic ZIF-8 without metallic core, although this can be removed by centrifugation. The important role of CTAB in avoiding the aggregation of Au TOHs and facilitate the growth of ZIF-8 was confirmed when the Au TOH was redispersed in pure water, resulting in a variety of nanostructures, from bare uncovered Au TOHs to aggregated Au TOHs coated with large ZIF-8 (Figure S17d). In addition, an EDX mapping was performed to confirm the elemental distribution of the Au TOH@ZIF-8 structures (Figure S18).

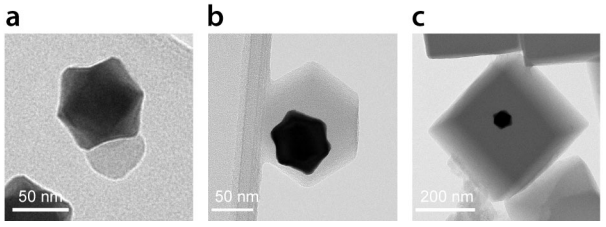

Figure 6. TEM images of representative Au TOH@ZIF-8 particles at different times of the encapsulation. The samples were extracted at (a) 15 min, (b) 60 min, and (c) 1 day after the start of the synthesis.

3.5. Surface-Enhanced Raman Spectroscopy. Au TOHs have been reported to exhibit excellent SERS activities due to their well-defined tips, edges, steps, and kinks, showing large electromagnetic field enhancement.[25,62] Interestingly, previous work from C.J. Murphy's group[38] on colloidal suspensions of Au nanorods and later Zhang et al.[26] on Au concave nanocubes and Au TOHs studied at single-particle SERS level, revealed that the maximum SERS signals were obtained on samples whose LSPR plasmon band position was blue-shifted in wavelength with respect to the excitation laser. To attest the SERS efficiency of the Au TOHs and find the optimal size for an excitation laser of 633 nm, we synthetically tailored three Au TOH samples so their plasmonic wavelengths were located preferably in the blue-shift zone of the 633 nm. The as-prepared Au TOHs were first functionalized

https://doi.org/10.1021/acsanm.4c00455
ACS Appl. Nano Mater. 2024, 7, 5598–5609

with the Raman active molecules, 2-NaT, on their surfaces, and then diluted into different volumes of Milli-Q water for the SERS measurements in solution. The particle concentrations of these samples can be calculated by determining the extinction intensities and cross sections (see details in Section 7.1 in the Supporting Information), we thus measured the extinction spectra of all the samples (Figure 7). The plasmonic peaks of these three Au TOH samples are at 596 nm (Au TOH 1), 619 nm (Au TOH 2), and 646 nm (Au TOH 3). The peak intensities are summarized in Table S5.

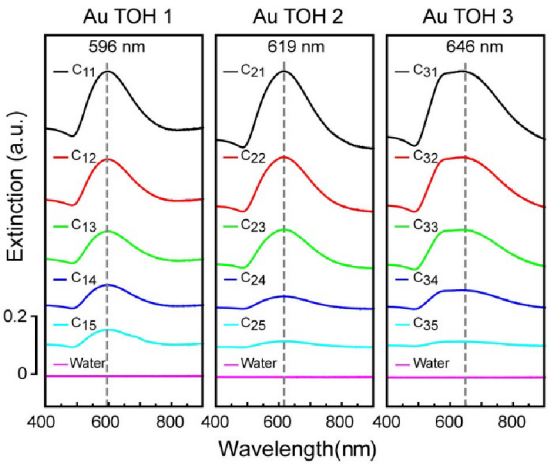

Figure 7. Extinction spectra of three Au TOH samples with 5 different colloidal solution concentrations (notation $C_{i,j}$ reads as sample i, concentration j). Vertical dashed line marks the LSPR peak, around the 633 nm laser excitation wavelength.

The SERS activities were evaluated by collecting the Raman spectra of 2-NaT absorbed on the Au TOHs, whose details are described in the experimental section. As displayed in Figure 8a, several characteristic signals were observed in the Raman spectra. Typically, the peaks located at 1382.8 and 1619.2 cm^{-1} are attributed to the ring modes, the C−H bending mode is located at 1069 cm^{-1}, and the peak at 769.3 cm^{-1} is dominated by the ring deformation.[63,64] It is seen that the intensities of these peaks slowly decreased with the reduction of the particle concentrations because of the decrease in the total number of measured molecules. The peak at 1382.8 cm^{-1} was selected to investigate the variations of the peak intensity as the change of particle concentration (Table S5).[65] The integrated area of the peak was plotted as a function of the peak intensity of extinction spectrum (Figure 8b), observing a linear dependency. Interestingly, sample Au TOH 1 and Au TOH 2 show similar slopes, which are the two samples with LSPR peaks blue-shifted from the laser wavelength. Sample Au TOH 1 exhibits a slightly higher Raman signal among these three samples when they have the same extinction intensity, result that can be explained as variations of the particle concentration, since Au TOH 1 being the smallest particle with smallest cross section,[66] it must have the largest particle concentration for a given extinction intensity (according to eq 3 in the Supporting Information). It is worth noting that since the lowest extinction intensity was 0.0156 for Au TOH 3, and with a cross section calculated from FEM simulation of 9.90×10^4 nm^2, the lowest detected particle concentration is 3.63×10^7 NP mL^{-1}. The detection limit in liquid is able to be improved by increasing the laser power and/or the integration time. In view of the similar slopes for sample Au TOH 1 and Au TOH 2, we considered pertinent to also calculate the enhancement factor (EF) of the Raman signals for these three samples by measuring the Raman signal of 0.1 M 2-NaT solution without Au nanoparticles and using eq 7 in the Supporting Information (Figure S19). The calculated EFs resulted to be 2.15×10^5, 2.56×10^5, and 1.72×10^5 for Au TOH 1, Au TOH 2, and Au TOH 3, respectively. In this case, the Au TOH 2 with LSPR peak at 619 nm and blue-shifted with respect the excitation light, presents a significantly higher EF when compared to the other two samples, which supports our previous observation and highlights the importance of synthetically tuning the plasmon peak to gain the maximum sensitivity in SERS applications.[26,38]

3.6. Refractive Index Sensing. LSPR properties of noble metal nanocrystals are sensitive to changes in the refractive index of the surrounding medium. An increase in the refractive index induces a red shift in the plasmonic peak of noble metal nanostructures, especially nanostructures with sharp tips and edges that exhibit strong sensitivities. Au TOHs have 14 sharp

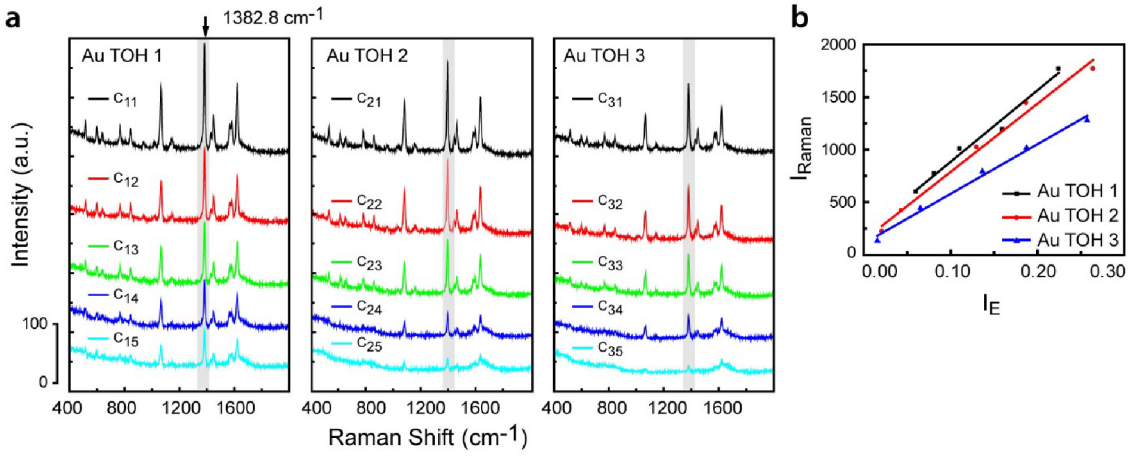

Figure 8. (a) SERS spectra of three Au TOH samples of different sizes, at 5 different colloidal concentrations, with absorbed 2-NaT molecules. Notation $C_{i,j}$ reads as sample i, concentration j. The vertical gray shadow line marks the Raman peak used for analysis. (b) Plots of the integrated area of Raman peak (I_{Raman}) at 1382.8 cm^{-1} as a function of the extinction intensity of the dipolar plasmonic peak in the extinction spectra (I_E). The coefficient values (R^2) of the linear fit are 0.976, 0.985, and 0.989, for Au TOH 1, Au TOH 2, and Au TOH 3, respectively.

https://doi.org/10.1021/acsanm.4c00455
ACS Appl. Nano Mater. 2024, 7, 5598−5609

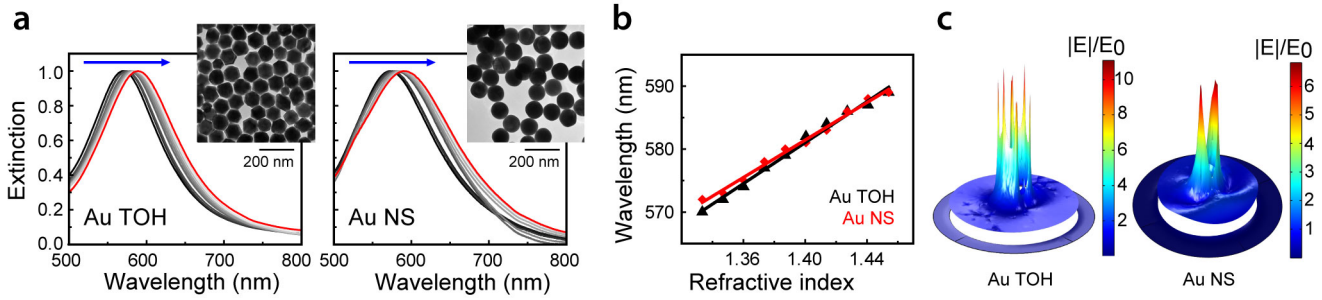

Figure 9. (a) Normalized extinction spectra of colloidal solutions of Au TOHs and Au NSs dispersed in water−glycerol mixtures of varying compositions. Representative TEM images of the samples are presented as insets. To appreciate the transition during changes in composition, the black line corresponds to colloids dispersed into water, and the red line corresponds to the solution with the highest concentration of glycerol. The blue arrow indicates the direction of increasing refractive index. (b) Plots of the LSPR peaks versus refractive index of the surrounding medium for Au TOHs and Au NSs. (c) Calculated electric field enhancement contours of an individual Au TOH (size, 56 nm) and a single Au NS (diameter, 56 nm) by FEM simulation.

tips and 24 edges, making it a suitable candidate for sensing variations in refractive index, which have interesting biosensing potential.[4,67,68] For this study, we evaluated the refractive index sensitivity of Au TOHs and compared it with that of Au NSs since both of them have high geometric symmetry and only one dipolar plasmonic peak located in the range between 500 and 800 nm. We prepared Au TOH and Au NS samples that possess similar LSPR peaks, located at 570 and 572 nm, respectively (Figure 9a), sized 96 ± 8 and 103 ± 3 nm, respectively (insets in Figures 9a, and S20). Bulk sensitivity measurements were performed by dispersing the Au nanoparticle samples into liquid mediums with different refractive indices. As the refractive index of the surrounding medium increased, the extinction spectra of the as-prepared samples gradually red-shifted (Figure 9a), as expected. The variations in the LSPR peak positions were plotted as a function of the refractive index, exhibiting good linear fits (Figure 9b). The refractive index sensitivities, determined by the slopes of the fitting lines, are 158 and 141 nm/RIU for Au TOHs and Au NSs, respectively. Au TOHs exhibit only a slightly higher refractive index sensitivity, which is likely related to the size difference since Au TOHs are about 7 nm smaller than Au NSs despite them having similar plasmonic peak positions. Therefore, we also synthesized two more Au TOH samples with larger average sizes (and closer to the Au NS size) to determine their refractive index sensitivity (Figure S21). The results confirmed that the sensitivity is largely determined by the sizes as well, with larger nanoparticles having higher sensitivities (Figure S22). Generally, a good sensor also needs to have a large value of figure-of-merit (FOM), which is defined as the refractive index sensitivity divided by the full width at half-maximum of the LSPR peak.[68] The FOM values for Au TOHs and Au NSs were calculated to be 1.38 and 1.06, respectively, again supporting Au TOHs as better candidates for refractive index sensing applications than Au NSs.

In Figure 9c, the simulated electric field for an Au TOH and an Au NS with the same size (56 nm) is illustrated. Plasmonic nanostructures have the ability to concentrate incident light into deeply subwavelength volumes resulting in large local field enhancements that can be several times that of the external field magnitude.[69] The field enhancement, defined as the ratio between the local field and the external field magnitudes, is the factor that drives the enhancement of light matter interaction because the higher it is, the larger the interaction. As a result, the typical signal required for refractive index sensing or nonlinear sensing, such as SERS, can be considerably reduced in such structures. To reveal the potential of our structures in this sense, we calculated the local field enhancements $f = |E|/|E_0|$ on Figure 9c, where $|E|$ is the amplitude of the local field and $|E_0|$ is the amplitude of the incident field. This was done by solving Maxwell's equations with COMSOL Multiphysics for the nanostructures under plane wave illumination. As can be seen, the Au NS exhibits values of f as high as 7 that occur at the interfaces of the particle. These hot spots are aligned with the polarization of the incident electric field. The f values of the TOH particle can be as high as 10 near the tips of the TOH structure. Moreover, there are more spots probed near the particle for the TOH in comparison to the NS, making it a better candidate for sensing and SERS. These simulation results further confirm that Au TOHs exhibit better potential for SERS and sensing than Au NSs. With a value of $f = 10$ near the TOH tips, the sensitivity to the SERS signal is expected to be enhanced by a factor $f^2 = 100$ per particle in comparison to bulk Raman scattering signals.

4. CONCLUSIONS

We have presented a simple and fast method to grow uniform Au TOHs with high shape yields and narrow size distributions for SERS and refractive index sensing. The experiments of monitoring the growth process confirmed that the entire process can be completed in less than 10 min, thanks to a fast growth process and the use of seeds without the need for aging treatment. We also conducted a series of optimizing experiments, including the addition of H_2PtCl_6, the concentration and types of surfactants, and the amount of AA, and analyzed their effects. Moreover, we were able to tailor Au TOH size by simply controlling the amount of seed solution used in the growth step, offering a remarkable range of Au TOH sizes from 39 to 268 nm with a narrow size distribution, which allows to fine-tune the LSPR properties. In addition, by varying the growth temperature, the dihedral angle can be gradually increased from 161°, which means the Miller indices of the facets of the obtained nanostructures can be tuned. We also presented a method to obtain Au TOH@ZIF-8 core−shell structure that will broaden the applicability of these structures to SERS fields such as gas sensing. The efficient SERS performance of Au TOHs in liquids was demonstrated, with SERS EFs of 10^5, and the importance of the LSPR peak position to optimize their sensitivity was also highlighted. When evaluating the refractive index sensitivity, we have

https://doi.org/10.1021/acsanm.4c00455
ACS Appl. Nano Mater. 2024, 7, 5598−5609

proved that Au TOHs are better candidates than Au NSs for sensing. Consequently, this fast, simple, and robust synthetic method will motivate the use of this high-indexed structure, paving the way to explore further applications in sensing, catalysis, and biomedicine.

■ ASSOCIATED CONTENT

Supporting Information

The Supporting Information is available free of charge at https://pubs.acs.org/doi/10.1021/acsanm.4c00455.

The details of how to determine the Miller index of the exposed facets of Au TOHs; results for the optimization of the synthetic conditions; the additional microscopy images of tuning sizes and Miller indices; HRTEM images of seeds; complementary SEM images of Au TOH@ZIF-8 and EDX mapping; calculations for determining the particle concentration, and the refractive index sensitivities of different sizes of Au TOH samples (PDF)

Movie S1 − Projection tilt series for an assembly of 4 Au TOHs recorded in bright field imaging mode of the electron microscope used to reconstruct the 3D volume (AVI)

Movie S2 − Reconstructed volume of Au TOHs using ART algorithm (AVI)

■ AUTHOR INFORMATION

Corresponding Author

Aleix G. Güell − *Laboratory of Physics of Interfaces and Thin Films, CNRS, UMR7647, Ecole Polytechnique, Institut Polytechnique de Paris, Palaiseau 91128, France;* orcid.org/0000-0002-0905-4131; Email: aleix.guell@polytechnique.edu

Authors

Guili Zhao − *Laboratory of Physics of Interfaces and Thin Films, CNRS, UMR7647, Ecole Polytechnique, Institut Polytechnique de Paris, Palaiseau 91128, France*

Florian Lochon − *Univ. Bordeaux, CNRS, CRPP, UMR5031, Pessac 33600, France*

Kassiogé Dembélé − *Laboratory of Physics of Interfaces and Thin Films, CNRS, UMR7647, Ecole Polytechnique, Institut Polytechnique de Paris, Palaiseau 91128, France*

Ileana Florea − *Laboratory of Physics of Interfaces and Thin Films, CNRS, UMR7647, Ecole Polytechnique, Institut Polytechnique de Paris, Palaiseau 91128, France; CRHEA, CNRS, Université Cote d'Azur, Valbonne 06560, France*

Alexandre Baron − *Univ. Bordeaux, CNRS, CRPP, UMR5031, Pessac 33600, France; Institut Universitaire de France, Paris Cedex 05 75231, France;* orcid.org/0000-0003-0697-6410

Razvigor Ossikovski − *Laboratory of Physics of Interfaces and Thin Films, CNRS, UMR7647, Ecole Polytechnique, Institut Polytechnique de Paris, Palaiseau 91128, France;* orcid.org/0000-0002-7084-7579

Complete contact information is available at: https://pubs.acs.org/10.1021/acsanm.4c00455

Author Contributions

The manuscript was written through contributions of all authors. All authors have given approval to the final version of the manuscript.

Notes

The authors declare no competing financial interest.

■ ACKNOWLEDGMENTS

This work was supported by the European Research Council (ERC Starting Grant Agreement No. ERC-StG-716641-AQUARAMAN to A.G.G.). G.Z. also thanks Prof. Cedric Tard, Prof. Kees Van Der Beek, and Ms Sylvie Coussot for their help. A.B. and F.L. acknowledge support from the French National Research Agency (ANR) in the frame of the project Plasmoglaz (ANR-18-CE05-0038). All the electron microscopy analyses were done at CIMEX (Centre Interdisciplinaire de Microscopie Electronique de l'X), which is gratefully acknowledged.

■ ABBREVIATIONS

AA, L-ascorbic acid; CTAB, cetyltrimethylammonium bromide; CTAC, cetyltrimethylammonium chloride; EDX, energy-dispersive X-ray spectrometry; EF, enhancement factor; FEM, finite-element method; FOM, figure-of-merit; HAADF, high-angle annular dark-field; HRTEM, high-resolution transmission electron microscopy; LSPR, local surface plasmon resonance; 2-MeIm, 2-methylimidazole; MOF, metal organic framework; 2-NaT, 2-naphthalenethiol; NS, nanosphere; RIU, refractive index unit; SAED, selected area electron diffraction; SEM, scanning electron microscopy; SERS, surface-enhanced Raman spectroscopy; STEM, scanning transmission electron microscopy; TEM, transmission electron microscopy; TOH, trisoctahedron; ZIF−8, zeolitic imidazolate framework

■ REFERENCES

(1) Scarabelli, L.; Sun, M.; Zhuo, X.; Yoo, S.; Millstone, J. E.; Jones, M. R.; Liz-Marzán, L. M. Plate-Like Colloidal Metal Nanoparticles. *Chem. Rev.* **2023**, *123* (7), 3493−3542.

(2) Zhang, H.; Chen, Y.; Chui, K. K.; Zheng, J.; Ma, Y.; Liu, D.; Huang, Z.; Lei, D.; Wang, J. Synthesis of Bitten Gold Nanoparticles with Single-Particle Chiroptical Responses. *Small* **2023**, *19* (26), 2301476.

(3) Jiang, R.; Li, B.; Fang, C.; Wang, J. Metal/Semiconductor Hybrid Nanostructures for Plasmon-Enhanced Applications. *Adv. Mater.* **2014**, *26* (31), 5274−5309.

(4) Mayer, K. M.; Hafner, J. H. Localized Surface Plasmon Resonance Sensors. *Chem. Rev.* **2011**, *111* (6), 3828−3857.

(5) Hu, M.; Chen, J.; Li, Z.-Y.; Au, L.; Hartland, G. V.; Li, X.; Marquez, M.; Xia, Y. Gold nanostructures: Engineering their plasmonic properties for biomedical applications. *Chem. Soc. Rev.* **2006**, *35* (11), 1084−1094.

(6) Elancheliyan, R.; Dezert, R.; Castano, S.; Bentaleb, A.; Nativ-Roth, E.; Regev, O.; Barois, P.; Baron, A.; Mondain-Monval, O.; Ponsinet, V. Tailored self-assembled nanocolloidal Huygens scatterers in the visible. *Nanoscale* **2020**, *12* (47), 24177−24187.

(7) Many, V.; Dézert, R.; Duguet, E.; Baron, A.; Jangid, V.; Ponsinet, V.; Ravaine, S.; Richetti, P.; Barois, P.; Tréguer-Delapierre, M. High optical magnetism of dodecahedral plasmonic meta-atoms. *Nanophotonics* **2018**, *8* (4), 549−558.

(8) Roach, L.; Lermusiaux, L.; Baron, A.; Tréguer-Delapierre, M. Symmetric plasmonic nanoparticle clusters: Synthesis and novel optical properties. In *Encyclopedia of Nanomaterials*; 1st ed., Yin, Y.; Lu, Y.; Xia, Y., Eds.; Elsevier, 2023; pp 113−127.

(9) Ma, Y.; Kuang, Q.; Jiang, Z.; Xie, Z.; Huang, R.; Zheng, L. Synthesis of Trisoctahedral Gold Nanocrystals with Exposed High-Index Facets by a Facile Chemical Method. *Angew. Chem., Int. Ed.* **2008**, *47* (46), 8901−8904.

(10) Xiong, Y.; Wiley, B. J.; Xia, Y. Nanocrystals with Unconventional Shapes-A Class of Promising Catalysts. *Angew. Chem., Int. Ed.* **2007**, *46* (38), 7157−7159.

(11) Li, Q.; Zhuo, X.; Li, S.; Ruan, Q.; Xu, Q.-H.; Wang, J. Production of Monodisperse Gold Nanobipyramids with Number Percentages Approaching 100% and Evaluation of Their Plasmonic Properties. *Adv. Opt. Mater.* **2015**, *3* (6), 801−812.
(12) Xie, J.; Zhang, Q.; Lee, J. Y.; Wang, D. I. C. The Synthesis of SERS-Active Gold Nanoflower Tags for In Vivo Applications. *ACS Nano* **2008**, *2* (12), 2473−2480.
(13) Hong, J. W.; Lee, S.-U.; Lee, Y. W.; Han, S. W. Hexoctahedral Au Nanocrystals with High-Index Facets and Their Optical and Surface-Enhanced Raman Scattering Properties. *J. Am. Chem. Soc.* **2012**, *134* (10), 4565−4568.
(14) Chiu, C.-Y.; Chung, P.-J.; Lao, K.-U.; Liao, C.-W.; Huang, M. H. Facet-Dependent Catalytic Activity of Gold Nanocubes, Octahedra, and Rhombic Dodecahedra toward 4-Nitroaniline Reduction. *J. Phys. Chem. C* **2012**, *116* (44), 23757−23763.
(15) Nikoobakht, B.; El-Sayed, M. A. Preparation and Growth Mechanism of Gold Nanorods (NRs) Using Seed-Mediated Growth Method. *Chem. Mater.* **2003**, *15* (10), 1957−1962.
(16) Jia, H.; Fang, C.; Zhu, X.-M.; Ruan, Q.; Wang, Y.-X. J.; Wang, J. Synthesis of Absorption-Dominant Small Gold Nanorods and Their Plasmonic Properties. *Langmuir* **2015**, *31* (26), 7418−7426.
(17) Li, C.; Shuford, K. L.; Chen, M.; Lee, E. J.; Cho, S. O. A Facile Polyol Route to Uniform Gold Octahedra with Tailorable Size and Their Optical Properties. *ACS Nano* **2008**, *2* (9), 1760−1769.
(18) Niu, W.; Zheng, S.; Wang, D.; Liu, X.; Li, H.; Han, S.; Chen, J.; Tang, Z.; Xu, G. Selective Synthesis of Single-Crystalline Rhombic Dodecahedral, Octahedral, and Cubic Gold Nanocrystals. *J. Am. Chem. Soc.* **2009**, *131* (2), 697−703.
(19) Wy, Y.; Jung, H.; Hong, J. W.; Han, S. W. Exploiting Plasmonic Hot Spots in Au-Based Nanostructures for Sensing and Photocatalysis. *Acc. Chem. Res.* **2022**, *55* (6), 831−843.
(20) Huo, D.; Ding, H.; Zhou, S.; Li, J.; Tao, J.; Ma, Y.; Xia, Y. Facile synthesis of gold trisoctahedral nanocrystals with controllable sizes and dihedral angles. *Nanoscale* **2018**, *10* (23), 11034−11042.
(21) Zhang, L.; Niu, W.; Xu, G. Synthesis and applications of noble metal nanocrystals with high-energy facets. *Nano Today* **2012**, *7* (6), 586−605.
(22) Xia, Y.; Xia, X.; Peng, H.-C. Shape-Controlled Synthesis of Colloidal Metal Nanocrystals: Thermodynamic versus Kinetic Products. *J. Am. Chem. Soc.* **2015**, *137* (25), 7947−7966.
(23) Quan, Z.; Wang, Y.; Fang, J. High-Index Faceted Noble Metal Nanocrystals. *Acc. Chem. Res.* **2013**, *46* (2), 191−202.
(24) Yu, Y.; Zhang, Q.; Lu, X.; Lee, J. Y. Seed-Mediated Synthesis of Monodisperse Concave Trisoctahedral Gold Nanocrystals with Controllable Sizes. *J. Phys. Chem. C* **2010**, *114* (25), 11119−11126.
(25) Song, Y.; Miao, T.; Zhang, P.; Bi, C.; Xia, H.; Wang, D.; Tao, X. {331}-Faceted trisoctahedral gold nanocrystals: synthesis, superior electrocatalytic performance and highly efficient SERS activity. *Nanoscale* **2015**, *7* (18), 8405−8415.
(26) Zhang, Q.; Large, N.; Wang, H. Gold Nanoparticles with Tipped Surface Structures as Substrates for Single-Particle Surface-Enhanced Raman Spectroscopy: Concave Nanocubes, Nanotrisoctahedra, and Nanostars. *ACS Appl. Mater. Interfaces* **2014**, *6* (19), 17255−17267.
(27) Yu, Y.; Zhang, Q.; Liu, B.; Lee, J. Y. Synthesis of Nanocrystals with Variable High-Index Pd Facets through the Controlled Heteroepitaxial Growth of Trisoctahedral Au Templates. *J. Am. Chem. Soc.* **2010**, *132* (51), 18258−18265.
(28) Wu, H.-L.; Kuo, C.-H.; Huang, M. H. Seed-Mediated Synthesis of Gold Nanocrystals with Systematic Shape Evolution from Cubic to Trisoctahedral and Rhombic Dodecahedral Structures. *Langmuir* **2010**, *26* (14), 12307−12313.
(29) Eguchi, M.; Mitsui, D.; Wu, H.-L.; Sato, R.; Teranishi, T. Simple Reductant Concentration-Dependent Shape Control of Polyhedral Gold Nanoparticles and Their Plasmonic Properties. *Langmuir* **2012**, *28* (24), 9021−9026.
(30) Zhang, Q.; Large, N.; Nordlander, P.; Wang, H. Porous Au Nanoparticles with Tunable Plasmon Resonances and Intense Field Enhancements for Single-Particle SERS. *J. Phys. Chem. Lett.* **2014**, *5* (2), 370−374.
(31) Chen, Q.-Q.; Hou, R.-N.; Zhu, Y.-Z.; Wang, X.-T.; Zhang, H.; Zhang, Y.-J.; Zhang, L.; Tian, Z.-Q.; Li, J.-F. Au@ZIF-8 Core−Shell Nanoparticles as a SERS Substrate for Volatile Organic Compound Gas Detection. *Anal. Chem.* **2021**, *93* (19), 7188−7195.
(32) Lafuente, M.; De Marchi, S.; Urbiztondo, M.; Pastoriza-Santos, I.; Pérez-Juste, I.; Santamaría, J.; Mallada, R.; Pina, M. Plasmonic MOF Thin Films with Raman Internal Standard for Fast and Ultrasensitive SERS Detection of Chemical Warfare Agents in Ambient Air. *ACS Sens.* **2021**, *6* (6), 2241−2251.
(33) Hu, P.; Zhuang, J.; Chou, L.-Y.; Lee, H. K.; Ling, X. Y.; Chuang, Y.-C.; Tsung, C.-K. Surfactant-Directed Atomic to Mesoscale Alignment: Metal Nanocrystals Encased Individually in Single-Crystalline Porous Nanostructures. *J. Am. Chem. Soc.* **2014**, *136* (30), 10561−10564.
(34) Gordon, R.; Bender, R.; Herman, G. T. Algebraic Reconstruction Techniques (ART) for three-dimensional electron microscopy and X-ray photography. *J. Theor. Biol.* **1970**, *29* (3), 471−481.
(35) Mastronarde, D. N. Dual-Axis Tomography: An Approach with Alignment Methods That Preserve Resolution. *J. Struct. Biol.* **1997**, *120* (3), 343−352.
(36) MessaoudiI, C.; Boudier, T.; Sorzano, C. O. S.; Marco, S. TomoJ: Tomography software for three-dimensional reconstruction in transmission electron microscopy. *BMC Bioinf.* **2007**, *8* (1), 288.
(37) Johnson, P. B.; Christy, R. W. Optical Constants of the Noble Metals. *Phys. Rev. B* **1972**, *6* (12), 4370−4379.
(38) Sivapalan, S. T.; DeVetter, B. M.; Yang, T. K.; van Dijk, T.; Schulmerich, M. V.; Carney, P. S.; Bhargava, R.; Murphy, C. J. Off-Resonance Surface-Enhanced Raman Spectroscopy from Gold Nanorod Suspensions as a Function of Aspect Ratio: Not What We Thought. *ACS Nano* **2013**, *7* (3), 2099−2105.
(39) Ruan, Q.; Shao, L.; Shu, Y.; Wang, J.; Wu, H. Growth of Monodisperse Gold Nanospheres with Diameters from 20 to 220 nm and Their Core/Satellite Nanostructures. *Adv. Opt. Mater.* **2014**, *2* (1), 65−73.
(40) Van Hove, M. A.; Somorjai, G. A. A new microfacet notation for high-Miller-index surfaces of cubic materials with terrace, step and kink structures. *Surf. Sci.* **1980**, *92* (2), 489−518.
(41) Cheref, Y.; Lochon, F.; Daugas, L.; Cleret de Langavant, C.; Larquet, É.; Baron, A.; Gacoin, T.; Kim, J. Dual-Band LSPR of Tungsten Bronze Nanocrystals Tunable over NIR and SWIR Ranges. *Chem. Mater.* **2022**, *34* (21), 9795−9802.
(42) Lermusiaux, L.; Many, V.; Barois, P.; Ponsinet, V.; Ravaine, S.; Duguet, E.; Tréguer-Delapierre, M.; Baron, A. Toward Huygens' Sources with Dodecahedral Plasmonic Clusters. *Nano Lett.* **2021**, *21* (5), 2046−2052.
(43) Sánchez-Iglesias, A.; Winckelmans, N.; Altantzis, T.; Bals, S.; Grzelczak, M.; Liz-Marzán, L. M. High-Yield Seeded Growth of Monodisperse Pentatwinned Gold Nanoparticles through Thermally Induced Seed Twinning. *J. Am. Chem. Soc.* **2017**, *139* (1), 107−110.
(44) Brailsford, A. D.; Wynblatt, P. The dependence of ostwald ripening kinetics on particle volume fraction. *Acta Metall.* **1979**, *27* (3), 489−497.
(45) Fang, C.; Zhao, G.; Xiao, Y.; Zhao, J.; Zhang, Z.; Geng, B. Facile Growth of High-Yield Gold Nanobipyramids Induced by Chloroplatinic Acid for High Refractive Index Sensing Properties. *Sci. Rep.* **2016**, *6* (1), 36706.
(46) Kim, J.; Yoo, S.; Kim, J.-M.; Choi, S.; Kim, J.; Park, S.-J.; Park, D.; Nam, J.-M.; Park, S. Synthesis and Single-Particle Surface-Enhanced Raman Scattering Study of Plasmonic Tripod Nanoframes with Y-Shaped Hot-Zones. *Nano Lett.* **2020**, *20* (6), 4362−4369.
(47) Liz-Marzán, L. M.; Grzelczak, M. Growing anisotropic crystals at the nanoscale. *Science* **2017**, *356* (6343), 1120−1121.
(48) Langille, M. R.; Personick, M. L.; Zhang, J.; Mirkin, C. A. Defining Rules for the Shape Evolution of Gold Nanoparticles. *J. Am. Chem. Soc.* **2012**, *134* (35), 14542−14554.

https://doi.org/10.1021/acsanm.4c00455
ACS Appl. Nano Mater. 2024, 7, 5598−5609

(49) Zhang, J.; Langille, M. R.; Personick, M. L.; Zhang, K.; Li, S. Y.; Mirkin, C. A. Concave Cubic Gold Nanocrystals with High-Index Facets. *J. Am. Chem. Soc.* **2010**, *132*, 14012−14014.
(50) Lohse, S. E.; Burrows, N. D.; Scarabelli, L.; Liz-Marzán, L. M.; Murphy, C. J. Anisotropic Noble Metal Nanocrystal Growth: The Role of Halides. *Chem. Mater.* **2014**, *26* (1), 34−43.
(51) Personick, M. L.; Langille, M. R.; Zhang, J.; Harris, N.; Schatz, G. C.; Mirkin, C. A. Synthesis and Isolation of {110}-Faceted Gold Bipyramids and Rhombic Dodecahedra. *J. Am. Chem. Soc.* **2011**, *133* (16), 6170−6173.
(52) Motl, N. E.; Smith, A. F.; DeSantis, C. J.; Skrabalak, S. E. Engineering plasmonic metal colloids through composition and structural design. *Chem. Soc. Rev.* **2014**, *43* (11), 3823−3834.
(53) Fang, C.; Jia, H.; Chang, S.; Ruan, Q.; Wang, P.; Chen, T.; Wang, J. (Gold core)/(titania shell) nanostructures for plasmon-enhanced photon harvesting and generation of reactive oxygen species. *Energy Environ. Sci.* **2014**, *7* (10), 3431−3438.
(54) Wang, H.; Halas, N. J. Mesoscopic Au "Meatball" Particles. *Adv. Mater.* **2008**, *20* (4), 820−825.
(55) Gao, C.; Vuong, J.; Zhang, Q.; Liu, Y.; Yin, Y. One-step seeded growth of Au nanoparticles with widely tunable sizes. *Nanoscale* **2012**, *4* (9), 2875−2878.
(56) Khlebtsov, N. G. Determination of Size and Concentration of Gold Nanoparticles from Extinction Spectra. *Anal. Chem.* **2008**, *80* (17), 6620−6625.
(57) Kou, X.; Ni, W.; Tsung, C.-K.; Chan, K.; Lin, H.-Q.; Stucky, G. D.; Wang, J. Growth of Gold Bipyramids with Improved Yield and Their Curvature-Directed Oxidation. *Small* **2007**, *3* (12), 2103−2113.
(58) Chow, T. H.; Li, N.; Bai, X.; Zhuo, X.; Shao, L.; Wang, J. Gold Nanobipyramids: An Emerging and Versatile Type of Plasmonic Nanoparticles. *Acc. Chem. Res.* **2019**, *52* (8), 2136−2146.
(59) Phan-Quang, G. C.; Yang, N.; Lee, H. K.; Sim, H. Y. F.; Koh, C. S. L.; Kao, Y.-C.; Wong, Z. C.; Tan, E. K. M.; Miao, Y.-E.; Fan, W.; Liu, T.; Phang, I. Y.; Ling, X. Y. Tracking Airborne Molecules from Afar: Three-Dimensional Metal−Organic Framework-Surface-Enhanced Raman Scattering Platform for Stand-Off and Real-Time Atmospheric Monitoring. *ACS Nano* **2019**, *13* (10), 12090−12099.
(60) Zheng, G.; de Marchi, S.; López-Puente, V.; Sentosun, K.; Polavarapu, L.; Pérez-Juste, I.; Hill, E. H.; Bals, S.; Liz-Marzán, L. M.; Pastoriza-Santos, I.; Pérez-Juste, J. Encapsulation of Single Plasmonic Nanoparticles within ZIF-8 and SERS Analysis of the MOF Flexibility. *Small* **2016**, *12* (29), 3935−3943.
(61) Pan, Y.; Heryadi, D.; Zhou, F.; Zhao, L.; Lestari, G.; Su, H.; Lai, Z. Tuning the crystal morphology and size of zeolitic imidazolate framework-8 in aqueous solution by surfactants. *CrystEngComm* **2011**, *13* (23), 6937−6940.
(62) Xu, Q.; Liu, W.; Li, L.; Zhou, F.; Zhou, J.; Tian, Y. Ratiometric SERS imaging and selective biosensing of nitric oxide in live cells based on trisoctahedral gold nanostructures. *Chem. Commun.* **2017**, *53* (11), 1880−1883.
(63) Roca, M.; Haes, A. J. Silica−Void−Gold Nanoparticles: Temporally Stable Surface-Enhanced Raman Scattering Substrates. *J. Am. Chem. Soc.* **2008**, *130* (43), 14273−14279.
(64) Zhu, D.; Wang, Z.; Zong, S.; Chen, H.; Chen, P.; Cui, Y. Wavenumber−intensity joint SERS encoding using silver nanoparticles for tumor cell targeting. *RSC Adv.* **2014**, *4* (105), 60936−60942.
(65) Zhuo, X.; Henriksen-Lacey, M.; Jimenez de Aberasturi, D.; Sánchez-Iglesias, A.; Liz-Marzán, L. M. Shielded Silver Nanorods for Bioapplications. *Chem. Mater.* **2020**, *32* (13), 5879−5889.
(66) van Dijk, M. A.; Tchebotareva, A. L.; Orrit, M.; Lippitz, M.; Berciaud, S.; Lasne, D.; Cognet, L.; Lounis, B. Absorption and scattering microscopy of single metal nanoparticles. *Phys. Chem. Chem. Phys.* **2006**, *8* (30), 3486−3495.
(67) Marinakos, S. M.; Chen, S.; Chilkoti, A. Plasmonic Detection of a Model Analyte in Serum by a Gold Nanorod Sensor. *Anal. Chem.* **2007**, *79* (14), 5278−5283.
(68) Gao, B.; Wang, Y.; Zhang, T.; Xu, Y.; He, A.; Dai, L.; Zhang, J. Nanoscale Refractive Index Sensors with High Figures of Merit via Optical Slot Antennas. *ACS Nano* **2019**, *13* (8), 9131−9138.
(69) Schuller, J. A.; Barnard, E. S.; Cai, W.; Jun, Y. C.; White, J. S.; Brongersma, M. L. Plasmonics for extreme light concentration and manipulation. *Nat. Mater.* **2010**, *9* (3), 193−204.

https://doi.org/10.1021/acsanm.4c00455
ACS Appl. Nano Mater. 2024, 7, 5598−5609